Mapping ice-shelf flow with interferometric synthetic aperture radar stacking

Mapping ice-shelf flow with interferometric synthetic aperture radar stacking

Malcolm McMILLAN,[1,2] Andrew SHEPHERD,[1] Noel GOURMELEN,[3] Jeong-Won PARK,[4] Peter NIENOW,[2] Eero RINNE,[5] Amber LEESON[1]

[1] *School of Earth and Environment, University of Leeds, Leeds, UK*
E-mail: m.mcmillan@leeds.ac.uk
[2] *School of GeoSciences, University of Edinburgh, Edinburgh, UK*
[3] *Ecole et Observatoire des Sciences de la Terre, University of Strasbourg, Strasbourg, France*
[4] *Earth System Sciences, Yonsei University, Seoul, Republic of Korea*
[5] *Finnish Meteorological Institute, Helsinki, Finland*

ABSTRACT. Interferometric synthetic aperture radar (InSAR) observations of ice-shelf flow contain ocean-tide and atmospheric-pressure signals. A model-based correction can be applied, but this method is limited by its dependency upon model accuracy, which in remote regions can be uncertain. Here we describe a method to determine two-dimensional ice-shelf flow vectors independently of model predictions of tide and atmospheric pressure, by stacking conventional and multiple aperture InSAR (MAI) observations of the Dotson Ice Shelf, West Antarctica. In this way we synthesize a longer observation period, which enhances long-period (flow) displacement signals, relative to rapidly varying (tide and atmospheric pressure) signals and noise. We estimate the error associated with each component of the velocity field to be $\sim$22 m a^{-1}, which could be further reduced if more images were available to stack. With the upcoming launch of several satellite missions, offering the prospect of regular short-repeat SAR acquisitions, this study demonstrates that stacking can improve estimates of ice-shelf flow velocity.

1. INTRODUCTION

Around the coastline of Antarctica, ice shelves provide an interface through which ice is melted by the ocean and the relatively warm coastal air. Through this connection, changes in atmospheric (Vaughan and Doake, 1996) and oceanic (Rignot and Jacobs, 2002; Shepherd and others, 2004) conditions can trigger an ice-shelf response which, over decadal timescales, can propagate a dynamic instability hundreds of kilometres inland (Payne and others, 2004). These changes can affect the mass balance of glaciological catchments (Shepherd and others, 2002; Wingham and others, 2009) and, as a consequence, can accelerate sea-level rise. Evidence of the dynamic response of inland ice to changing ice-shelf conditions has been observed at several locations on the Antarctic Peninsula and the Amundsen Sea sector of the West Antarctic ice sheet (Rott and others, 2002; Shepherd and others, 2002; De Angelis and Skvarca, 2003; Rignot and others, 2004, 2005; Scambos and others, 2004; Pritchard and others, 2009). These studies demonstrate how external perturbations in climate can lead to changes in Antarctic ice sheet (AIS) mass over relatively short time periods. Several studies have documented ice-shelf acceleration prior to collapse (Rignot and others, 2004; Vieli and others, 2007). These highlight the importance of monitoring ice-shelf flow velocities, both as an indicator of the stability of the glaciological catchment, and in providing details of the processes through which ice shelves interact with the atmosphere, the ocean and grounded ice upstream (Joughin and Padman, 2003; Payne and others, 2007; Vieli and others, 2007). Until such mechanisms are well understood, the AIS contribution to future sea-level rise remains uncertain.

Over the last two decades, conventional satellite-based interferometric synthetic aperture radar (InSAR) has provided precise, spatially extensive measurements of ice velocity (e.g. Goldstein and others, 1993; Joughin and others, 1995, 1996; Kwok and Fahnestock, 1996; Rignot, 1996; Lang and others, 2004; Rignot and others, 2008). This technique measures displacement in the satellite's line of sight, and so the signal returned from the surface of an ice shelf contains components due both to ice flow (assumed here to be in the horizontal plane) and vertical motion (Goldstein and others, 1993; Rignot, 1996; Rignot and MacAyeal, 1998; Rignot and others, 2000). Over the (typically daily) timescales at which InSAR measurements are best made, vertical displacement deriving both from tidal motion and from changes in atmospheric pressure can be significant relative to the speed at which the ice flows (Rignot and others, 2000; Padman and others, 2003). Consequently, these signals must be removed in order to determine ice flow velocity with confidence. The response of an ice shelf to atmospheric pressure fluctuations is commonly modelled as an inverted barometer (Padman and others, 2003) and termed the 'inverse barometer effect' (IBE). While this method has been used to isolate the tidal component of altimetry observations (Padman and others, 2008), no studies have attempted to model and remove this component of the InSAR signal when estimating ice-shelf flow. In the case of the tidal component, a tide model is commonly used to simulate this part of the interferometric signal (computed from the difference in tide height at the acquisition times of the two SAR images) (e.g. Rignot and Jacobs, 2002; Joughin and others, 2003; Rignot and others, 2004; Vieli and others, 2006). However, in remote Antarctic regions this method is limited by two factors: (1) modelling tides is challenging, because tide-gauge, bathymetric and altimetry data are scarce (Egbert and others, 1994; King and Padman, 2005) and (2) in the absence of in situ data, it is

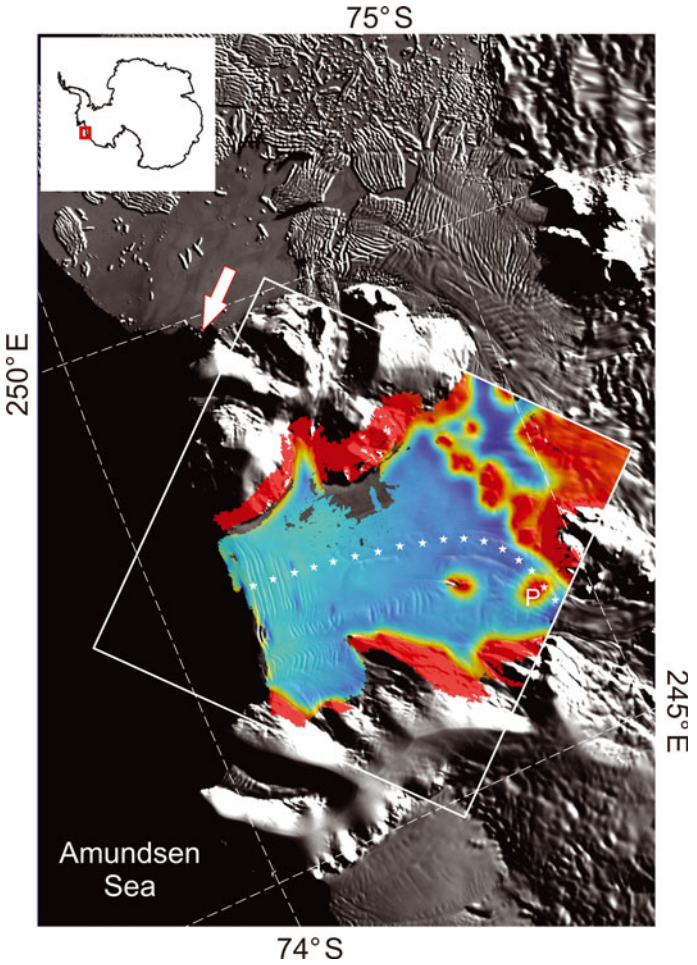

Fig. 1. The Dotson Ice Shelf. Colour scale shows pattern of non-steady (tidal and IBE) displacement, derived from differential InSAR; red indicates grounded ice, blue indicates floating ice. White box shows the spatial extent of the SAR data frames used in this study. White arrow indicates the satellite across-track direction. White dots indicate the location of the transect shown in Figure 5, and P indicates the position of the pinning point identified in Figure 5. The background image is taken from the Moderate Resolution Imaging Spectroradiometer (MODIS) Mosaic of Antarctica (Haran and others, 2006).

difficult to assess precisely the ability of a model to predict changes in tide height over the period of interferometric acquisition (McMillan and others, 2011). As a consequence, the extent to which unmodelled tidal motion affects these ice-shelf flow velocity estimates is uncertain.

Stacking interferograms is routinely used to map solid Earth topography (Sandwell and Price, 1998; Sandwell and Sichoix, 2000) and ground deformation (Zebker and others, 1997; Wright and others, 2001; Gourmelen and Amelung, 2005). When mapping surface deformation, stacking enables a longer observation period to be utilized, so the magnitude of unwanted atmospheric, orbital and topographic signals is reduced, relative to the steady rate of deformation. Here we apply this technique to the problem of mapping ice-shelf flow; by stacking we minimize unwanted short-period tidal and IBE signals, relative to the steady flow signal. As a consequence, we do not rely on tide or IBE model predictions to map ice-shelf flow speeds, and hence eliminate the requirement that any single model realization of tidal or IBE displacement is sufficiently accurate (or of known accuracy). As with solid Earth applications, by stacking we also reduce atmospheric, orbital and topographic noise.

Stacking interferograms to minimize the tidal component of ice-shelf displacement was originally proposed by Rignot and MacAyeal (1998) in a study of the Filchner–Ronne Ice Shelf. To date, however, mapping ice-shelf flow using this approach has primarily been limited by the lack of long sequences of regular, short-repeat SAR acquisitions, which lend themselves to this technique. The recent European Remote-sensing Satellite (ERS-2) 3 day campaign and the planned Sentinel-1 and RADARSAT Constellation satellites offer the prospect of the provision of such data. With a view to these missions, we revisit the ERS data archive to provide a detailed demonstration and assessment of the technique at the Dotson Ice Shelf, in the Amundsen Sea sector of West Antarctica. Specifically, we (1) extend the stacking method so as to resolve two-dimensional (2-D) velocity vectors from data acquired from a single viewing direction, by utilizing conventional and multiple aperture interferometry, (2) use model statistics to quantify the residual tidal and IBE error in our stacked velocity solution, (3) compare our results with flow predictions determined using a traditional method whereby model predictions are used to remove the tidal and IBE signals and (4) assess the wider application of a stacking-based approach to future satellite missions.

2. STUDY AREA

The Dotson Ice Shelf (Fig. 1) spans an area of $\sim$3400 km^2 and is one of several small ice shelves situated along the Amundsen Sea coastline of the West Antarctic ice sheet. This region, which contains sufficient ice to raise sea levels by $\sim$1.5 m, currently has the greatest mass deficit of all of Antarctica (Shepherd and Wingham, 2007). In the last two decades, satellite observations of this region have revealed ice-shelf thinning (Shepherd and others, 2004) and grounding-line retreat (Rignot, 1998, 2002). Additionally, grounded ice upstream has thinned (Shepherd and others, 2002; Pritchard and others, 2009; Wingham and others, 2009) and accelerated (Rignot, 2008). The changes in this region are likely to have been driven by high rates of ice-shelf basal melting, resulting from the intrusion of warm Circumpolar Deep Water into sub-ice-shelf cavities (Jacobs and others, 1996; Thoma and others, 2008; Jenkins and others, 2010), via seabed troughs that run across the continental shelf (Nitsche and others, 2007; McMillan and others, 2009). Satellite observations indicate that between 1992 and 2001 the Dotson Ice Shelf was thinning at an average rate of $3.3 \pm 0.4\,\mathrm{m\,a^{-1}}$ (Shepherd and others, 2004). Once other factors affecting surface lowering had been accounted for (namely temporal fluctuations in sea-level height, ocean density, ice-shelf density, surface mass accumulation and ice mass flux divergence), Shepherd and others (2004) estimated that an average net basal melt rate of $\sim 8\,\mathrm{m\,a^{-1}}$ was required to produce this rate of thinning.

3. DATA

The principal dataset used in this study to demonstrate the stacking method was a sequence of SAR images acquired by ERS-1. These data were processed using a range of techniques to provide measurements of ice-shelf flow. As part of the InSAR processing, a digital elevation model (DEM) and laser altimetry data were used to remove unwanted

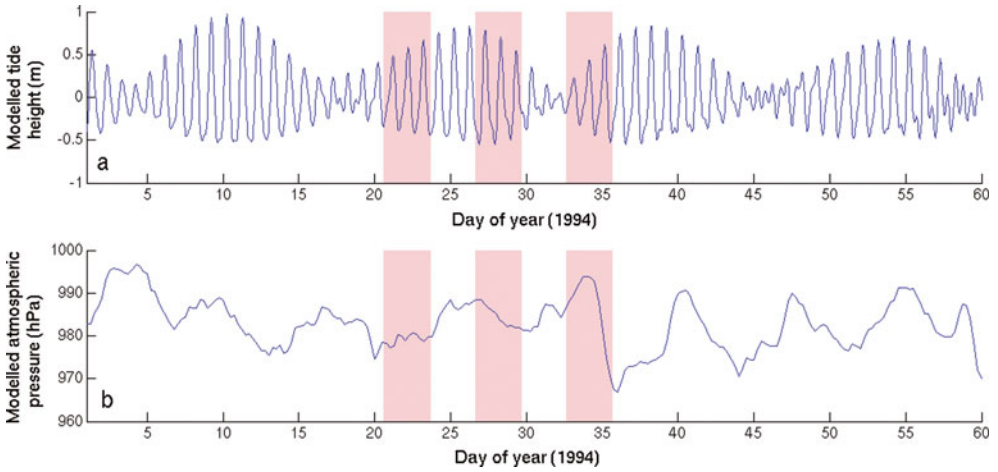

Fig. 2. (a) Modelled tide height and (b) modelled surface level atmospheric pressure at the Dotson Ice Shelf during the period of SAR data acquisition. Tide heights were estimated at 74.1° S, 247.5° E using the FES2004 tide model (Lyard and others, 2006). Atmospheric pressure was estimated at 74° S, 247° E using the ERA-40 reanalysis (Uppala and others, 2005). Shaded areas indicate periods over which interferograms were formed.

signals from the SAR data. To determine the errors associated with the stacking technique, and to provide a more general assessment of our proposed method, we have used data from tide and atmospheric pressure models to simulate other forms of ice-shelf motion. Further details of these data are given below.

3.1. Synthetic aperture radar

To map ice-shelf flow we used SAR data acquired during the second ice phase of ERS-1 (Table 1). The SAR data were obtained in raw format and processed using the Gamma software package (Werner and others, 2001). We used a 5 km Antarctic-wide DEM (Bamber and Bindschadler, 1997) to remove the topographic component of the interferometric phase. To refine the ERS-1 interferometric geometry, we used point (60 m diameter) measurements of elevation from the Geoscience Laser Altimeter System (GLAS), on board the Ice, Cloud and land Elevation Satellite (ICESat) (Zwally and others, 2002). These data were acquired during the period 2003–07. We used GLAS Level 1B elevation data (GLA06), which include corrections for atmospheric propagation delays and the effect of solid Earth tides (Brenner and others, 2003). Data points with no saturation elevation correction or large receiver gain values (>50) were discarded. Saturation correction was added to the elevations. Geolocations in the GLA06 dataset were used without additional corrections.

3.2. Tide model

To model the tidal motion of the Dotson Ice Shelf, we used the finite-element solution model FES2004 (Lyard and others, 2006), which performs well in the Amundsen Sea (McMillan and others, 2011). FES2004 is a global tide model, with 1/8° resolution, which utilizes sparse Antarctic tide-gauge data (<10 records), together with TOPEX/Poseidon and ERS altimetry. The model was used for two purposes: (1) to generate tidal predictions coincident with the acquisition of our SAR data and (2) to compute the distribution of tidal signals from a year-long, hourly-resolution model run. Tide heights were obtained from the model just seaward of the ice front, at 74.1° S, 247.5° E, as we believe they are more accurate at that location (McMillan and others, 2011) than under the ice shelf itself, where water column thicknesses are poorly known. The modelled tide height during the period of SAR data acquisition is shown in Figure 2a.

3.3. Surface-level atmospheric pressure

In the absence of in situ meteorological data, model data from the European Centre for Medium-Range Weather Forecasts (ECMWF) ERA-40 reanalysis (Uppala and others, 2005) were used to determine surface-level atmospheric pressure changes at the Dotson Ice Shelf. Data at 74° S, 247° E were extracted from a $1° \times 1°$ regularly spaced grid (derived from an N80 reduced Gaussian grid), which was acquired from the British Atmospheric Data Centre at 6 hourly temporal resolution. These model data were used in two ways: (1) to generate predictions of surface-level atmospheric pressure coincident with the acquisition of our SAR data (via a linear interpolation between the two closest 6 hourly model records) and (2) to compute the distribution

Table 1. SAR data used to form interferometric solutions. e1 signifies ERS-1 satellite; $B_\perp$ specifies the perpendicular baseline of the SAR image pair

Image pair (sensor-orbit-frame)	Acquisition date (reference image)	Temporal separation	Track	$B_\perp$	Usage	Interferogram identifier
e1-13153-5182 / e1-13196-5182	20 Jan 1994	3 days	39	17 m	InSAR + MAI	I1
e1-13239-5182 / e1-13282-5182	26 Jan 1994	3 days	39	−196 m	InSAR + MAI	I2
e1-13325-5182 / e1-13368-5182	1 Feb 1994	3 days	39	44 m	InSAR	I3

of pressure signals from a year-long model record. The modelled atmospheric pressure during the period of SAR data acquisition is shown in Figure 2b.

4. METHODS

In this section we describe (1) the methods used to generate stacked displacement maps, (2) the use of model statistics to estimate the associated tidal and IBE error and (3) the formation of comparison displacement maps using single model realizations to remove the predicted tidal and IBE signals from a single interferogram.

4.1. Conventional InSAR stacking

The conventional InSAR processing techniques used to map ice motion are well documented (Goldstein and others, 1993; Joughin and others, 1995, 1996; Kwok and Fahnestock, 1996; Rignot, 1996), so here we provide only a short overview of the methods used in this study. Interferograms were formed from co-registered SAR image pairs, with 3 days separating each acquisition (Table 1). This acquisition configuration was chosen to (1) minimize temporal decorrelation by keeping the interferometric temporal baseline short and (2) assess the method with respect to a simple and regular acquisition cycle. The sensitivity of our method to the temporal sampling provided by this acquisition cycle is examined below in Section 6.

For repeat-pass SAR observations of an ice shelf, the interferometric phase, φ, is due to a combination of terms:

$$\varphi = \varphi_{\text{flat}} + \varphi_{\text{topo}} + \varphi_{\text{flow}} + \varphi_{\text{tide}} + \varphi_{\text{ibe}} + \varphi_{\text{noise}} + \varphi_{\text{ref}} \quad (1)$$

This expression describes the spatial variation in phase, relative to a spatially constant reference or phase offset, φ_{ref}. Phase variations across the image are caused by (1) the changing viewing angle across the ground track, φ_{flat} (as described by the shape of Earth's ellipsoid), (2) surface topography, φ_{topo}, (3) surface displacement due to ice flow, φ_{flow}, tidal forcing, φ_{tide}, and the IBE, φ_{ibe}, and (4) noise in the received signal, φ_{noise}. The noise term encompasses both spatially correlated (e.g. atmospheric phase distortions) and uncorrelated (e.g. signal decorrelation) effects.

Firstly, we used the interferometric geometry to simulate and remove the 'flat Earth' signal. Where possible we used ICESat surface elevations over non-moving terrain to further refine our interferometric baseline estimate, and thus improve our model of this component of the signal. Where this was not possible, due to a lack of interferometric coherence over stationary regions, precise orbit information acquired from the Technical University of Delft, the Netherlands, was used. Loss of coherence over the period of interferogram acquisition was probably due to wind- or precipitation-driven changes to the near-surface snowpack.

Next, we unwrapped each interferogram. Ignoring the noise term (see Section 5.2) and the constant phase offset (which we address at the end of this section), the remaining variation in the interferometric phase comprises contributions from (1) topography and (2) the line-of-sight component of the various modes of surface displacement:

$$\varphi = -\frac{4\pi}{\lambda}\left[\frac{zB_{\perp}}{r\sin\theta} + \sin\psi\Delta h_{\text{flow}} + \cos\psi\left(\Delta z_{\text{tide}} + \Delta z_{\text{ibe}}\right)\right] \quad (2)$$

where λ is the radar wavelength (5.7 cm for the ERS-1 used in this study), $B_{\perp}$ is the component of the interferometric baseline perpendicular to the radar line of sight, z is the elevation of the target pixel above Earth's ellipsoid, r is the range from the satellite to the target pixel, θ is the radar look angle and ψ is the incidence angle of the radar beam relative to the normal to Earth's ellipsoid. Over the time period, Δt days, of the interferometric observation, Δh_{flow} denotes the horizontal ground range component of surface displacement due to ice flow, and Δz_{tide} and Δz_{ibe} denote the vertical displacement of the ice shelf in response to the tide and IBE, respectively. Stacking n interferograms yields a stacked phase:

$$\sum_{i=1}^{n}\varphi_i = -\frac{4\pi}{\lambda}\left[\frac{z}{r\sin\theta}\sum_{i=1}^{n}B_{\perp,i} + \sin\psi\sum_{i=1}^{n}\Delta h_{\text{flow},i} + \cos\psi\sum_{i=1}^{n}\left(\Delta z_{\text{tide},i} + \Delta z_{\text{ibe},i}\right)\right] \quad (3)$$

To isolate the surface displacement component, elevations from a DEM (Bamber and Bindschadler, 1997) were scaled by the effective perpendicular baseline of the stacked interferogram, and used to simulate and remove the topographic phase. Dividing the remaining stacked phase through by the total observation period of the stack yields an estimate of the ice flow velocity during that period (m d^{-1}), subject to error from residual tidal and IBE signals:

$$\frac{\sum_{i=1}^{n}\varphi_i}{\sum_{i=1}^{n}\Delta t_i} = -\frac{4\pi}{\lambda}\left[\sin\psi\frac{\sum_{i=1}^{n}\Delta h_{\text{flow},i}}{\sum_{i=1}^{n}\Delta t_i} + \cos\psi\frac{\sum_{i=1}^{n}\left(\Delta z_{\text{tide},i} + \Delta z_{\text{ibe},i}\right)}{\sum_{i=1}^{n}\Delta t_i}\right] \quad (4)$$

This expression forms the basis of this work, whereby we use the stacked phase to estimate horizontal ice flow, and model statistics to determine the magnitude of the associated tidal and IBE errors.

The method so far only determines relative displacement, i.e. how displacement varies across the image space. To determine absolute displacement values (by estimating the reference phase offset), we referenced our displacement map to a set of ~2700 displacement estimates acquired where ice was grounded. These reference displacements were determined using the technique of coherence tracking (mapping surface motion based upon optimizing coherence between patches of SAR image pairs; Derauw, 1999; Pattyn and Derauw, 2002; Strozzi and others, 2002). Specifically, we first identified grounded areas by differencing two interferograms (Hartl and others, 1994; Rignot, 1996, 2002). This removed the ice flow component of the phase signal common to both interferograms and isolated the non-steady motion associated with the ice-shelf response to tidal and atmospheric pressure forcing. Next, we adjusted our InSAR velocities so that the mean InSAR-derived velocity (over regions identified as being grounded) matched the equivalent velocity determined using coherence tracking. This approach allowed us to utilize a spatially extensive dataset to reference our InSAR-derived velocities.

4.2. Modelling tide and IBE error

Our stacked InSAR velocity solution does not utilize model predictions of tide or IBE to isolate ice-shelf flow. Instead we have aimed to minimize these signals by stacking displacement estimates. We now use the tide and IBE models to simulate the statistics of the residual tide and IBE signals, in order to quantify the associated error in our stacked predictions of flow (Eqn (4)). We formed time series from both the FES2004 tide model and the ERA-40 atmospheric pressure reanalysis for the entirety of 1994, at hourly and 6 hourly intervals, respectively. We converted atmospheric pressure changes into changes in ice-shelf height (IBE displacement) using an inverse barometer approximation, namely the ratio determined empirically by Padman and others (2003) of $-0.95\,\mathrm{cm\,hPa^{-1}}$. Padman and others (2003) found little variation in estimates of this ratio derived from data collected at three widely spaced and different-sized ice shelves, so we assume this estimate is valid at the Dotson Ice Shelf. Next, we calculated the tidal and IBE displacements that would occur in a stacked interferometric prediction acquired at every point along our time series. We converted these modelled vertical displacements into annual velocities in the satellite's across-track direction and so determined the distribution of velocity errors, arising from residual tidal and IBE signals, that could be present in our stacked prediction of flow.

4.3. Isolating flow displacement using model predictions

To assess our stacked velocity solution we used the same InSAR data (Table 1) to form alternative displacement maps, using the standard technique of removing the tidal signal from each individual interferogram, based upon the coincident tide model predictions (Rignot and Jacobs, 2002; Joughin and others, 2003; Rignot and others, 2004; Vieli and others, 2006). We have extended this method to additionally remove the modelled IBE component of ice-shelf motion. To isolate flow, we followed the interferometric method described above to convert individual interferograms into maps of absolute across-track displacement. Next, we used a double difference technique (Hartl and others, 1994; Rignot, 1996, 2002) to determine the pattern of non-steady (tide and IBE) displacement of the Dotson Ice Shelf (Fig. 1). To simulate the tidal and IBE signals occurring within each interferogram, we scaled the double difference solution so that the mean displacement across the freely floating portion of the ice shelf matched that of the combined modelled tide and IBE displacement. This prediction was subtracted from each conventional InSAR displacement map, in order to produce multiple predictions of ice flow.

4.4. Multiple aperture InSAR stacking

Conventional InSAR only measures one dimension of the displacement field: along the satellite's line of sight. To determine 2-D vectors we estimated displacement along the satellite track using multiple aperture InSAR (MAI) processing (Bechor and Zebker, 2006; Jung and others, 2009; Gourmelen and others, 2011). Previous work has shown that MAI offers improvements in estimates of along-track displacement, compared with tracking methods, both for solid Earth (Bechor and Zebker, 2006) and glaciological (Gourmelen and others, 2011) applications. MAI processing splits the antenna beam to form two sub-aperture single-look complex (SLC) images, one forward-looking and one backward-looking, from each conventional SAR image. Then, from a pair of SAR images, the forward-looking SLCs and the backward-looking SLCs are each combined to form two interferograms which are sensitive to displacement in both the azimuth and range directions. Differencing the interferometric phase of these forward- and backward-looking interferograms cancels the common range component of the interferometric phase and isolates a phase difference that is proportional to the along-track component of the displacement field. Because MAI is less sensitive to surface displacement than conventional InSAR (a 2π phase change corresponds to a 10 m change in displacement for MAI versus 2.8 cm for InSAR), phase gradients are lower, allowing the phase over moving and stationary areas to be linked. These stationary areas provide an absolute reference for our displacement estimates. Although MAI is insensitive to vertical ice-shelf motion, we still stack MAI interferograms, so as to amplify the steady ice flow signal, relative to temporally uncorrelated noise sources. Finally we combine the along-track velocity component from MAI with the across-track velocity component from conventional InSAR, in order to determine a map of velocity magnitude.

5. RESULTS

5.1. Stacked velocity map

We used the stacked multiple aperture and conventional InSAR solutions to determine the along-track (Fig. 3a) and across-track (Fig. 3b) components of our flow velocity vectors. We then combined these components to give a map of the magnitude of the 2-D flow velocity vectors (Fig. 3c). We assumed ice flow was in the horizontal plane, i.e. that the vertical component of flow was negligible. Our solution shows that the Dotson Ice Shelf is primarily fed by fast-flowing ice originating from Smith and Kohler Glaciers. Close to the grounding line, where the ice funnels through a narrow gap, velocities exceed $500\,\mathrm{m\,a^{-1}}$. Further downstream, on the freely floating portion of the ice shelf, speeds drop to $\sim 320\,\mathrm{m\,a^{-1}}$, before increasing again to $\sim 500\,\mathrm{m\,a^{-1}}$ close to the calving front.

5.2. Error assessment

To assess the viability of our stacking method, we considered the error associated with our stacked velocity solution. We define the error, ε, associated with interferometric estimates of horizontal ice-shelf flow as

$$\varepsilon^2 = \varepsilon^2_{\mathrm{tide}} + \varepsilon^2_{\mathrm{ibe}} + \varepsilon^2_{\mathrm{topo}} + \varepsilon^2_{\mathrm{base}} + \varepsilon^2_{\mathrm{atmos}} + \varepsilon^2_{\mathrm{coh}} + \varepsilon^2_{\mathrm{ref}} + \varepsilon^2_{\mathrm{unw}} \quad (5)$$

The error components refer, in left-to-right order, to errors from residual tidal displacement, residual IBE displacement, unmodelled topography, unmodelled baseline effects, atmospheric phase distortions, loss of coherence, error in determining an absolute reference and error in the phase-unwrapping process. To simplify this assessment, we assumed that all errors were independent. This provides a close approximation of the true error, since the dominant error components (namely tide and IBE, as outlined in this section) are independent. The extent to which these error sources affect the across- and along-track components of our displacement field varies as a consequence of the different techniques used. We address the error associated with each component in turn.

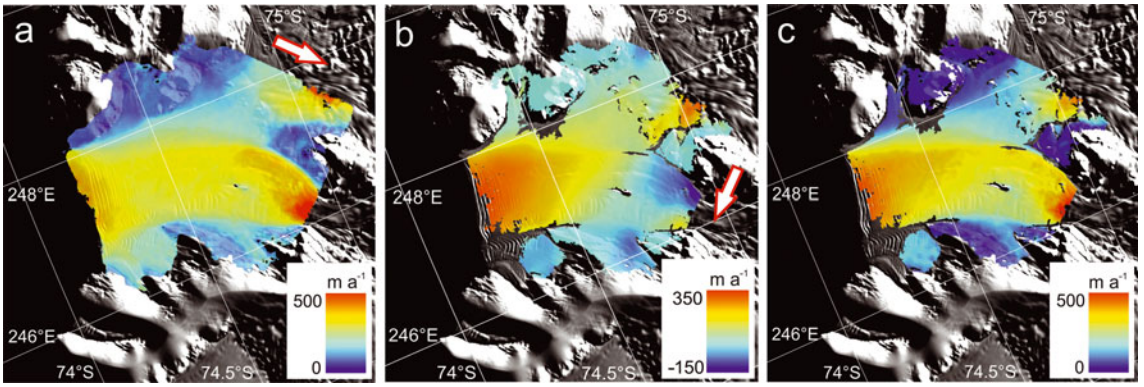

Fig. 3. Flow velocity of the Dotson Ice Shelf. (a) Along-track velocity component derived from stacked MAI; white arrow indicates the satellite along-track direction. (b) Across-track velocity component derived from stacked InSAR; white arrow indicates the satellite across-track direction. (c) Velocity magnitude from combined along-track (a) and across-track (b) components. The background image is taken from the MODIS Mosaic of Antarctica (Haran and others, 2006).

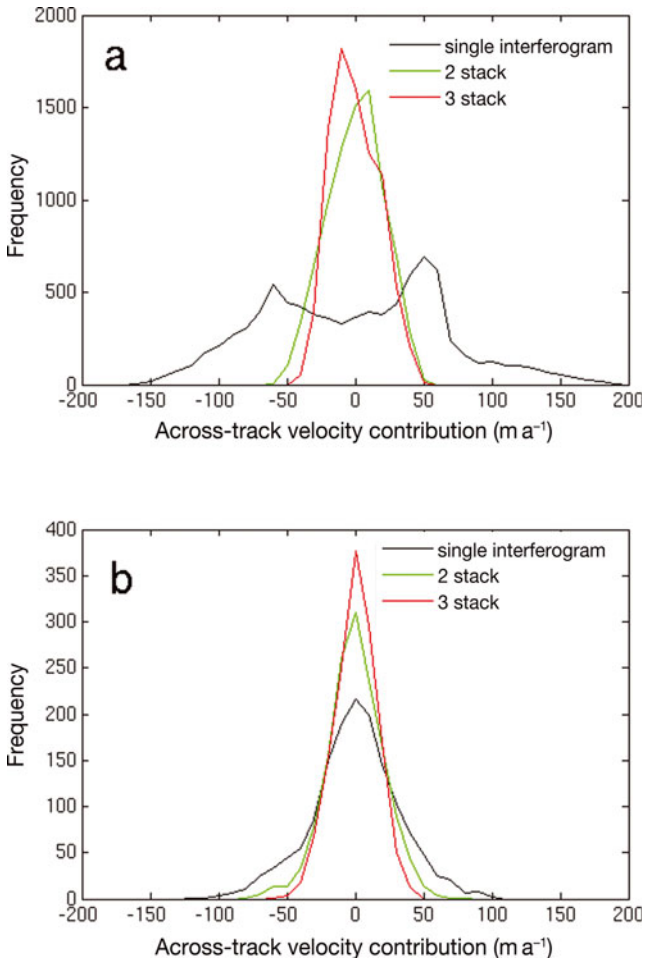

Fig. 4. Modelled distribution of (a) tidal and (b) IBE contributions to conventional InSAR estimates of across-track flow velocity at the Dotson Ice Shelf. Each panel shows the expected distribution of across-track velocity errors arising from the tidal and IBE motion of the ice shelf within a single interferogram (3 day separation), and for two- and three-stacked interferograms. Tide was computed from hourly realizations of the FES2004 tide model, and the IBE from 6 hourly realizations of the ERA-40 reanalysis of surface-level atmospheric pressure, converted into changes in ice-shelf height using the empirical relationship determined by Padman and others (2003). Both models were run for the entirety of 1994, and the resulting vertical displacements were converted into equivalent annual velocities in the satellite's across-track direction.

Conventional InSAR error

Firstly we considered the effect of each error component (Eqn (5)) on our conventional InSAR estimates of across-track displacement. To assess the tide and IBE errors ($\varepsilon_{\text{tide}}$ and ε_{ibe}) we used 1 year's worth of model data to estimate the distribution of these signals occurring over the timescales of our interferometric acquisitions, and converted these to equivalent errors in the across-track component of our velocity solution (Fig. 4). In each case we computed the signals corresponding to (1) a single interferogram (i.e. the 3 day difference in tide height), (2) two-stacked interferograms and (3) three-stacked interferograms. Both the tide and IBE contributions to the velocity error tend to diminish in size as the interferometric predictions are stacked, primarily as a consequence of the longer observation period over which displacement is measured. The distributions of the stacked tidal and IBE signals are roughly normal and centred close to zero. In contrast, the twin-peaked distribution of the single-interferogram tidal displacement indicates that, in a single interferogram, a much larger signal is likely to be present, and demonstrates the value of stacking to reduce the tidal contribution. To determine the contribution of these sources of error to our three-stack velocity estimate, we combined the standard deviations of the modelled tidal (20 cm vertical displacement over a 9 day period) and IBE (18 cm vertical displacement over a 9 day period) signals. This yielded a combined residual vertical motion of 27 cm, which equates to an error of 22 m a^{-1} in the across-track component of our stacked velocity solution.

To determine an absolute reference for our InSAR displacements, we matched the mean InSAR and mean tracking range displacements over grounded ice. Consequently, any bias in the tracking displacements is transferred to our InSAR solution. We estimated this referencing error, ε_{ref}, from the displacement values of pixels that were located on stationary areas. Over the 3 day period of our tracking measurements, the mean across-track displacement of these points was 5.9 cm, equivalent to a bias of 7 m a^{-1} in our velocity solution.

The effect of the remaining error terms upon our velocity solution is likely to be small in comparison to the aforementioned errors. Because of the minimal topographic relief in our study area, DEM errors are small (~5 m; Bamber and

Gomez-Dans, 2005) relative to the 70 m altitude of ambiguity (the elevation change equivalent to one complete cycle of the interferometric phase) of our stacked interferogram. This topographic error, $\varepsilon_{\text{topo}}$, equates to a 0.9 cm across-track displacement error in our 9 day stacked interferogram, equivalent to a 0.4 m a^{-1} error in our velocity estimate.

As a measure of the displacement error arising from loss of coherence, ε_{coh}, we calculated the errors associated with the average coherence of each interferogram (Rodriguez and Martin, 1992). The resulting displacement error in our 9 day stacked interferogram is 0.4 cm, equivalent to an error in the across-track component of our velocity solution of $<$0.2 m a^{-1}. Atmospheric distortions of the interferometric phase, $\varepsilon_{\text{atmos}}$, occur because of spatial and temporal inhomogeneity in the troposphere and ionosphere. To quantify the tropospheric component, we followed the procedure outlined by McMillan and others (2011). Based upon the length- and timescales appropriate to our study and the parameterization determined by Emardson and others (2003), we estimated the error arising from the tropospheric variability to be at most 4.1 cm in our 9 day stacked interferogram, equivalent to a 1.7 m a^{-1} error in our velocity solution. We neglected ionospheric errors (Gray and others, 2000), as these tend to manifest themselves as distinctive features and we do not see any evidence of these features in our dataset. We have aimed to minimize any unmodelled baseline effects by, where possible, refining our baseline estimates and checking for residual long-wavelength phase gradients over stationary areas. It is possible that some small residual baseline error may exist in our velocity solution, which we have not accounted for in our error budget. The process of stacking will, however, further reduce any such effect. During the phase-unwrapping process we unwrapped along a path that gave no visible unwrapping errors, so we assume no unwrapping errors in our velocity solution. The contributions from errors associated with our across-track displacement estimates are summarized in Table 2. Of these, the errors arising from atmospheric distortions and loss of coherence are specific to the C-band frequency of the ERS SAR and will vary for sensors operating at alternative frequencies. Combining all across-track error sources yields a 23 m a^{-1} error in this component of our velocity solution. This error component is dominated by the errors from tidal and IBE effects.

Table 2. Summary of terms contributing to displacement error in the three-stack (9 day) InSAR estimate of across-track displacement

Error term	Across-track error cm
Tide	41.0
Inverse barometer effect	36.9
Topography	0.9
Referencing	5.9
Atmosphere	4.1
Coherence	0.4
Total	55.6

Multiple-aperture InSAR error

We now consider the error contributions (Eqn (5)) to our MAI estimates of along-track displacement. As part of MAI processing, the forward- and backward-looking interferometric phases are differenced, so errors common to both viewing angles will cancel. These include topographic and tropospheric contributions (Bechor and Zebker, 2006), plus any signal associated with the vertical motion of the ice shelf. Unmodelled baseline errors (Jung and others, 2009) were estimated from phase trends over stationary areas and removed. A visual inspection again showed no evidence of ionosphere-related errors (Gray and others, 2000). Because MAI is less sensitive to surface displacement than conventional InSAR, fringe rates are lower, so we do not anticipate unwrapping errors will occur.

We estimated the remaining MAI error terms, that of loss of coherence, ε_{coh}, and of satisfactorily referencing displacements to stationary areas, ε_{ref}, from the displacement values of ~24 000 pixels that were located on non-moving ground. The displacements of these points exhibit an approximately normal distribution, with a root-mean-square error of 34 cm for our 6 day stacked pair, equivalent to an error of 21 m a^{-1} in the along-track component of our velocity field. To assess the MAI technique, we compared this estimate of MAI error with an equivalent error associated with displacements determined using coherence tracking. We found that MAI offered a ~30% improvement over coherence tracking.

We have determined that the errors associated with the across- and along-track components of our flow velocity solution are roughly equal (23 and 21 m a^{-1}, respectively); a consequence of (1) the improved along-track accuracy offered by stacking MAI images, as compared with conventional tracking methods, and (2) the effect of residual vertical motion upon InSAR estimates of across-track displacement. As such, we have demonstrated that 2-D ice-shelf velocity can be estimated by combining MAI and InSAR data acquired from a single viewing direction, with comparable errors pertaining to both the velocity vector components.

Velocity magnitude error

Commonly in studies of ice flow, it is estimates of velocity magnitude (Fig. 3c) that are of most interest. The simplest approach to determining the error associated with the velocity magnitude is to sum in quadrature the along-track and across-track error components, which yields an error of 31 m a^{-1} in our velocity magnitude solution. This approach assumes independence of along-track and across-track errors. The MAI and InSAR observations are both derived from the same SAR data, so the coherence and referencing errors affecting both velocity components will not necessarily be independent. However, because these errors form only a tiny fraction of the total InSAR error (Table 2), we expect any increase in the total error due to the non-independence of these components to be small. The extent to which the error vector (defined by the along- and across-track error components) affects the velocity magnitude will vary according to the orientation and magnitude of the velocity vector relative to the error vector. For a 2-D flow velocity vector, $\mathbf{v}$, with an associated error vector, $\mathbf{e}$, the change (i.e. error) in the velocity magnitude, $\varepsilon_{|\mathbf{v}|}$, resulting from the vector addition of $\mathbf{e}$ to $\mathbf{v}$, can be described using the cosine rule:

$$\varepsilon_{|\mathbf{v}|} = |\mathbf{v}+\mathbf{e}| - |\mathbf{v}| = \sqrt{|\mathbf{v}|^2 + |\mathbf{e}|^2 - 2|\mathbf{v}||\mathbf{e}|\cos\theta} - |\mathbf{v}| \quad (6)$$

If the vectors $\mathbf{v}$ and $\mathbf{e}$ are placed head to tail, then θ is the inner angle formed where they meet, such that when $\theta = 180^\circ$ the vectors $\mathbf{v}$ and $\mathbf{e}$ point in the same direction,

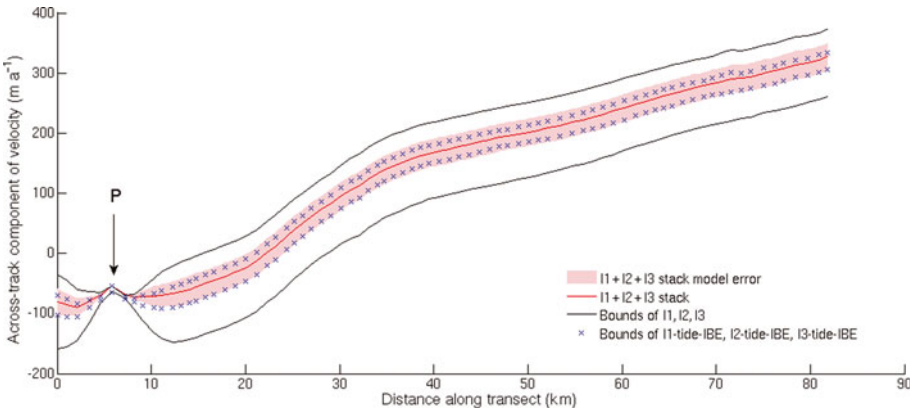

Fig. 5. Across-track component of the Dotson Ice Shelf flow speed (transect location marked in Fig. 1). P indicates a pinning point where the ice is grounded. Black curves indicate the maximum and minimum displacements of three interferograms (I1, I2 and I3; Table 1) which include tidal and IBE signals. Crosses indicate the range of these interferometric predictions of displacement, after modelled tide and IBE have been removed. Red curve indicates stacked prediction of displacement, with no use of tide or IBE models. Red shading indicates uncertainty of stacked prediction, determined from tide and IBE model statistics.

and $\theta = 0°$ indicates that **v** and **e** are orientated in opposite directions. The error in velocity magnitude peaks at 31 m a^{-1} when the velocity and error vectors are orientated in the same, or exactly opposite, direction. The quadrature sum of our along- and across-track error components therefore represents an upper bound upon the error associated with our velocity magnitude estimate. In more favourable cases the error in velocity magnitude will be significantly smaller, tending to zero when the velocity and error vectors are close to orthogonal. Consequently, a simple quadrature sum of the error components will often overestimate the true velocity magnitude error.

6. DISCUSSION

In this section we begin by comparing our stacking method to conventional InSAR methods for determining ice-shelf flow. With a view to upcoming satellite missions, we then assess the wider applicability of the method described here. We investigate (1) the sensitivity of the tidal and IBE signals to alternative temporal sampling regimes offered by other satellites and (2) the potential for larger image stacks to further reduce these errors.

6.1. Comparison of velocity predictions

Residual tidal and IBE displacements contribute the greatest error to our across-track velocity solution. To assess the impact of these two error sources upon our across-track velocity estimates, we compared our stacked map of across-track displacement to solutions obtained by a commonly used method (e.g. Rignot and Jacobs, 2002; Joughin and others, 2003; Rignot and others, 2004; Vieli and others, 2006), whereby model predictions are used to remove the tidal and IBE signals. We formed three velocity estimates by removing modelled tidal and IBE signals from each of the individual interferograms used in our stacking solution. Figure 5 shows a comparison of these solutions extracted from a transect along the primary line of ice flow (transect location shown in Fig. 1). We have plotted only the across-track component of velocity, as only this component is sensitive to vertical motion. Where ice is grounded (indicated by P in Figs 1 and 5) all velocity estimates converge. Because the InSAR solutions are tied down using all grounded locations (red in Fig. 1), and not just at point P, this convergence confirms that errors arising from unmodelled topography and baseline effects are small, and that flow remains steady over the period of data acquisition. Where the ice is freely floating (greater than ~10 km along the transect), each velocity estimate exhibits a roughly constant offset, which we interpret as resulting from vertical displacement due to the combined effect of the tide and IBE. The fact that this offset displays little spatial variation over the floating ice shelf indicates that our velocity estimates are not greatly affected by spatial variability in the tidal and IBE signals over the length scales of the ice shelf. This is consistent with the modelled IBE's spatial variability over the ice shelf at the times of data acquisition, which produces on average 3 m a^{-1} variation in the velocity signal. We do not perform an equivalent assessment for the tidal signal because the accuracy of the FES2004 model under the ice shelf is uncertain (McMillan and others, 2011). Assuming that these spatial patterns are uncorrelated in time, then stacking will further diminish the effects of any such spatial variability.

We compared InSAR velocity predictions before and after modelled tide and IBE corrections. Using model predictions to remove the tidal and IBE signals from each of the interferograms decreases the variability between each of the interferograms (blue crosses in Fig. 5), compared to the original interferograms (black curves in Fig. 5), and indicates that models successfully account for some of the tidal and IBE motion. However, some variation still exists, probably as a result of residual unmodelled vertical ice-shelf motion. This variation is indicative of the accuracy limits of tide and IBE model predictions. In contrast, our stacked velocity solution does not rely upon model predictions and consequently is not limited by the accuracy of these estimates. By utilizing stacking, we have maintained independence from model data, while achieving a velocity prediction that falls within the range of model-dependent solutions (i.e. the region bounded by the blue crosses in Fig. 5). This gives us confidence that, for the data used here, stacking only a small number of interferograms (three in this case) provides a reasonable, and model-independent, estimate of flow velocity. This study is, however, only based upon a relatively limited set of SAR data and we have no independent means of determining the actual tidal

and IBE displacement. Consequently, we cannot discount the possibility that, fortuitously, the tidal and IBE signals happened to cancel in our particular stacked prediction of flow, and in other instances our stacked solution may be more greatly affected by these signals. Our error model does, however, account for this uncertainty, because we have modelled the distribution of all potential tide and IBE errors. This provides a measure of the possible variation in our velocity solution, depending upon the particular tidal and IBE realization present in our data. The fact that we have only stacked relatively few interferograms is reflected in the spread of this distribution. We assess the magnitude of this error and the implications for our stacking method in Section 6.2.

6.2. Comparison of methods for error estimation

When ice-shelf flow velocities are determined from a single interferogram, together with a single model realization of tide and IBE displacement, then different image pairs produce varying velocity solutions (as shown by blue crosses in Fig. 5). This variation results from inaccuracies in model predictions of tidal and IBE displacements. Accordingly, the error assigned to such a velocity solution must account for the effect of these model inaccuracies. A direct model validation is difficult in remote areas, such as the Amundsen Sea where we know of only one attempt (McMillan and others, 2011) to assess the accuracy with which tide models can specifically reproduce the interferometric tidal displacement (Rignot (2002) assessed a model's ability to simulate the difference between two displacements, but not the displacement itself). While McMillan and others (2011) produced the first such accuracy estimate in the Amundsen Sea, imprecision inherent in the method used limited the estimate of the associated across-track velocity error to $22 \pm 17\,\mathrm{m\,a^{-1}}$. Consequently, the error associated with flow velocities determined from a single interferogram (blue crosses in Fig. 5) is not well constrained.

In contrast, because velocities derived using the stacking method are independent of model predictions, we avoid the problem of quantifying the associated model accuracy. In our method we do not use models to simulate and remove specific tidal and IBE displacements, but only to estimate the statistics of these signals, in order to assess the distribution of possible errors within our stacked velocity prediction. As such, we only require that the statistics of the model are sufficiently accurate; in other words, that the model simulates lifelike behaviour. A previous study (Shepherd and Peacock, 2003) found that tide model error was dominated by inaccuracies in predicting the tidal phase. Consequently, model statistics should adequately reflect the set of all tidal amplitudes, even if they do not correctly predict the timing at which a given amplitude occurs. The combined tidal and IBE error determined from model statistics for the stacked velocity solution is plotted in Figure 5. This assessment of error is consistent with the variability of solutions that utilize model predictions to remove the tidal and IBE signals, as would be expected, given that both the error associated with our stacked solution and the model error in predicting tidal and IBE displacement (McMillan and others, 2011) are $\sim 20\,\mathrm{m\,a^{-1}}$. By stacking only three interferograms, we have achieved an accuracy comparable to that provided by current tide models. Future satellite missions, offering the prospect of forming larger image stacks, have the potential to further reduce this stacked velocity error.

6.3. Generalization of stacking method

The results of this study indicate that, for the dataset considered here, stacking provides an effective method for reducing tidal and IBE errors, without using model predictions to remove these signals. Here we assess the wider applicability of this method by considering alternative sampling regimes, resulting from satellites with different orbit configurations. We also assess the potential for a further reduction of errors by stacking a larger number of images.

The motivation for this assessment is provided by the prospect of new data, from satellites which will make regular, short-repeat acquisitions that are well suited to this stacking method. In the first half of 2011, ERS-2 was placed into a 3 day acquisition cycle, thus providing a new set of data with the potential to create larger image stacks. Looking to the future, the planned launch of the Sentinel-1 and RADARSAT Constellation satellites offers the prospect of regular SAR acquisitions, albeit with different temporal sampling regimes, and with it the potential to create larger image stacks and further reduce tidal and IBE errors.

Sensitivity of tide and IBE to temporal sampling

This work has focused on a specific acquisition configuration: a series of interferograms formed from a regular 3 day acquisition cycle, such that the reference images of each interferogram are separated by 6 days (Table 1). Using this configuration we have modelled the distribution of tidal and IBE signals that could occur within our stacked interferogram. If, however, the tidal and IBE signals exhibit temporal structure, then the magnitude of these signals will vary according to the temporal sampling offered by the satellite. To assess this variability, we modelled the tidal and IBE signals for a range of sampling configurations. For each configuration, we modelled the signals in both a stack of three and a stack of five interferograms to investigate how the sensitivity was affected by the number of interferograms stacked. We varied both the temporal baseline of the interferogram (i.e. the separation between the two SAR images forming each interferogram) and the interferogram separation (i.e. the separation between each master image in the interferogram stack). Repeating the procedure described in Section 4, tide and IBE model statistics were calculated for each sampling regime. For every distribution, the standard deviation of the modelled signal associated with the image stack was converted into an equivalent error in the annual flow velocity. Results are shown in Figure 6.

In both stacks, the tidal and IBE signals tend to decrease as the temporal baseline increases. This is because of the decreasing influence of the tide and IBE, relative to the steady flow signal, as the observation period increases. With respect to the period of separation between interferograms in the stack, the tidal signal displays a clear structure (Fig. 6a and b), and exhibits considerable sensitivity to the time separation of interferograms. In both the stack of three interferograms (Fig. 6a) and the stack of five interferograms (Fig. 6b) the tidal signal peaks at a contribution of $\sim 70\,\mathrm{m\,a^{-1}}$ when interferograms are separated by a multiple of ~ 14 days. This is a consequence of the strong beating of the fortnightly (Mf) tidal constituent at our study site, which is clearly evident in the modelled tidal record (Fig. 2a), and which dominates the long period (greater than diurnal) tidal signal.

The sensitivity of the tidal signal to the temporal sampling regime implies that the repeat time of the satellite will

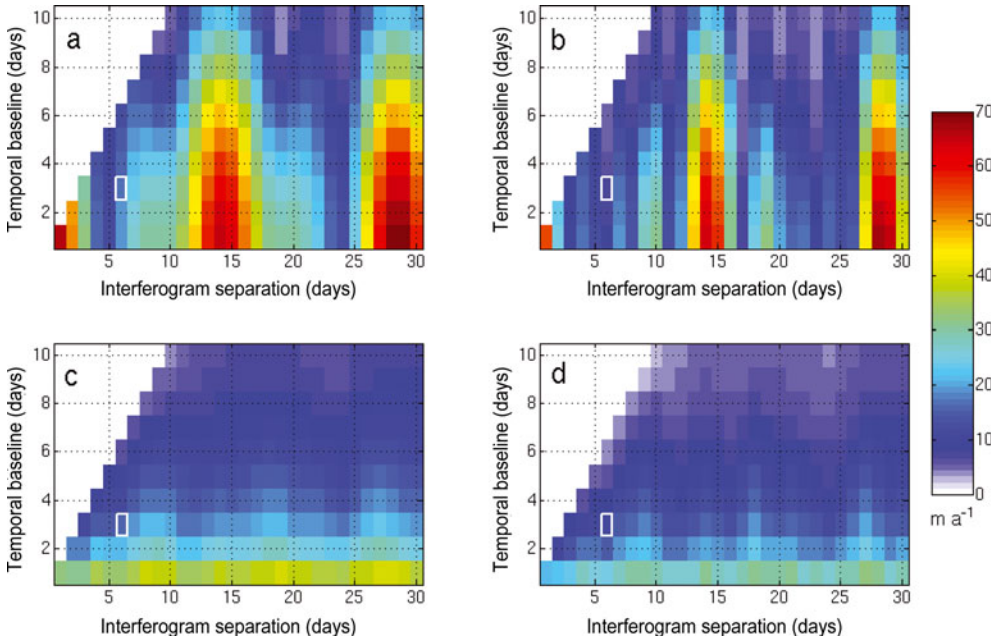

Fig. 6. Modelled sensitivity of (a, b) tidal and (c, d) IBE signals to the interferometric temporal sampling regime. Results are plotted for stacks of three interferograms ((a, c)) and five interferograms ((b, d)). Each plot shows the standard deviation of the modelled velocity error arising from the tide or IBE. Each standard deviation is calculated from the set of all modelled signals, obtained from a year-long model run, such as those shown in Figure 4. The temporal baseline specifies the time period separating the pair of SAR images used to form each interferogram; the interferogram separation indicates the elapsed time between the master images of consecutive interferograms in the stack. The white boxes mark the sampling regime used in this study. Interferogram separations shorter than the temporal baseline have been set to zero.

influence the effectiveness of the stacking technique. Worst-case errors occur where the sampling frequency matches that of the dominant long-period tidal constituent. In this case, stacking is unlikely to achieve the accuracy offered by a method that uses model predictions to remove the tidal and IBE signals. For the majority of sampling configurations, however, our analysis (Fig. 6) indicates that stacking will be an effective technique. The temporal sampling provided by the ERS acquisitions used in this study (indicated by white boxes in Fig. 6) proves favourable in producing a relatively small tidal signal. Furthermore, this analysis provides an indication of the effectiveness of stacking given the 6 day revisit time planned for Sentinel-1. For a continuous stack of 6 day interferograms (where the slave image of the preceding interferogram becomes the master image of the next interferogram), this analysis suggests that stacking five interferograms, and hence observing a full month-long period, would reduce the tidal error contribution to $\sim 5\,\mathrm{m\,a^{-1}}$.

In contrast to the tidal signal, the period of separation between the stacked interferograms has little effect upon the magnitude of the IBE signal (Fig. 6c and d). This is due to the lack of temporal structure in the atmospheric pressure record. Comparing the three-stack and five-stack scenarios, both the tidal and IBE error contributions tend to be lower in the five-stack, as a consequence of the longer period of observation. In the case of the tidal signal, the temporal structure is less well defined in the 5-stack; again a consequence of the longer total period of observation, which captures more completely the full tidal cycle.

Benefits offered by a larger stack

In this study the data archive has limited us to stacking only three regularly spaced interferograms. The ERS-2 2011 3 day acquisition phase and the planned Sentinel-1 and RADARSAT Constellation satellites offer the prospect of regular SAR acquisitions and with it the potential to stack a greater number of interferograms. To investigate the possible benefits offered by stacking a greater number of images we used the tide and atmospheric models to estimate the magnitude of these signals in larger stacks (again following the procedure described in Section 4). In particular, we considered three sampling scenarios: (1) the configuration used in this study (3 day interferograms, 6 days between each reference image in the interferogram stack); (2) a continuous series of observations from 3 day data (i.e. the slave image of the previous interferogram becomes the master image of the following interferogram); and (3) as in (2) but with 6 day repeat data (as planned for Sentinel-1). Results for up to ten stacked interferograms are shown in Figure 7. In all three sampling scenarios, the tidal and IBE errors decrease as a larger stack is formed; a consequence of the longer period of observation. The greatest benefit is gained with the first few interferograms that are stacked, particularly in the cases where interferograms are separated by 6 days, when simply stacking two interferograms reduces the tidal signal by two-thirds. As more interferograms are stacked, there is a general trend towards diminishing improvements, although the availability of a larger number of interferograms has the benefit of providing the opportunity to selectively choose interferograms, based upon criteria such as coherence and baseline characteristics.

Limitations and method development

The primary limitation of the stacking method is its high demand upon data. This was noted by Rignot and MacAyeal (1998) in their earlier assessment of this technique. In our study, for example, we have only been able to form a

relatively small stack of images, and there are insufficient usable data to be able to stack interferograms from a second viewing direction. For glaciological applications, the number of data suitable for stacking is limited by the relatively rapid time frame over which signal coherence is lost over ice. To date, stacking has primarily been used for solid Earth applications where surface displacements are relatively small and surface scatterers are relatively stable. This allows coherent interferograms to be formed over much longer time periods than is possible for glaciological applications and consequently provides a more extensive dataset to work with. Future satellite missions with regular short-repeat acquisitions will therefore particularly benefit glaciological applications, by providing longer image sequences that are suitable for stacking. Further improvements to the method described here may also be achieved by utilizing more sophisticated stacking regimes (e.g. Biggs and others, 2007), for example by including pixels that are only coherent in a subset of all interferograms in the stack.

Despite the limited data currently available, we find that stacking proves to be a valuable technique for mapping ice-shelf velocity, with only relatively few scenes required to reduce residual tidal errors to match the accuracy achievable with tide models in the Amundsen Sea (McMillan and others, 2011). This is aided by the satellite repeat time, which is exactly 3 days, and yields interferograms that are relatively insensitive to much of the high-amplitude, approximately diurnal cyclicity of the tides. As a consequence, the modelled standard deviation (from its ~0 mean) of the vertical 3 day tidal displacement is only 26 cm. Both tide model errors (King and Padman, 2005; King and others, 2011; McMillan and others, 2011) and tidal amplitudes in the Amundsen Sea are broadly comparable to most of Antarctica's coastal waters, with the exception of the Weddell Sea which experiences ~2–3 times the tidal range (Padman and others, 2002). Consequently, this study demonstrates that stacking is likely to be an effective method for mapping ice-shelf velocity around much of Antarctica. In the case of Weddell Sea ice shelves, or regions where other tidal constituents dominate, it may be necessary to stack more images to reduce the tidal signal to acceptable levels, or to use a combined approach that removes the modelled tidal signal from the stacked interferogram. Alternatively, tide model predictions could be used to guide future satellite acquisition schedules to periods of low tidal variability.

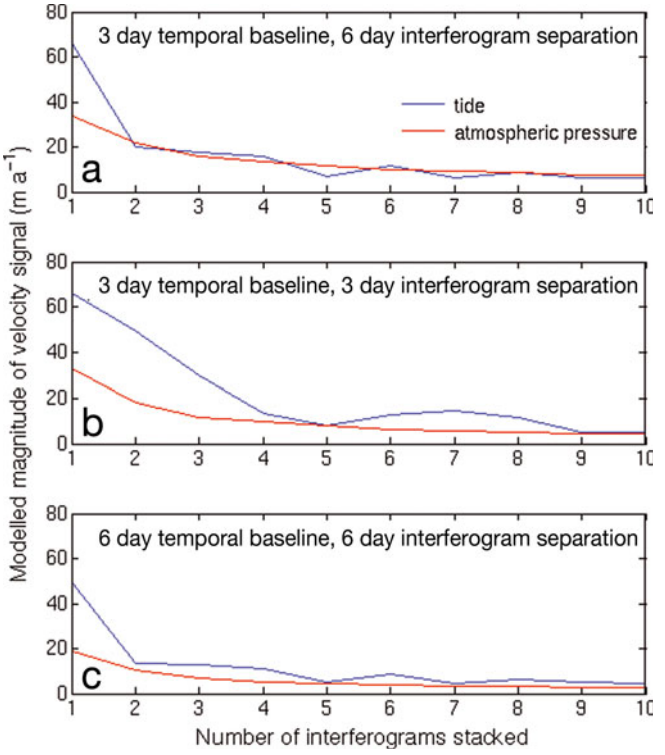

Fig. 7. Variation in the velocity error arising from modelled tidal and atmospheric pressure (IBE) signals, according to the number of interferograms stacked. Velocity error is dependent upon the temporal sampling regime (Fig. 6), so we show results for three configurations: (a) the configuration used in this study; (b) a continuous 3 day sampling configuration, where the slave image of each interferogram is used as the master image of the following interferogram; and (c) a continuous sampling configuration (as in (b)) but for a 6 day repeat cycle, as is planned for the Sentinel-1 satellites. Velocity errors are calculated from the standard deviation of the tidal and IBE signals, modelled over a year-long period.

7. CONCLUSIONS

This study demonstrates a method to map ice-shelf flow independently of tide and atmospheric-pressure model predictions. By stacking interferograms, we synthesize a longer observation period, and amplify the steady flow signal relative to other temporally varying signals, such as the vertical motion of an ice shelf in response to the tide and changing atmospheric pressure. Models, instead of being employed to isolate the flow signal, are used to simulate the distribution of residual tidal and IBE signals, and so provide a better constraint upon the remaining error in our velocity solution. By utilizing MAI processing, we have demonstrated that 2-D ice-shelf velocity can be estimated from InSAR data acquired from a single viewing direction.

We have stacked interferograms to map the ice flow velocity of the Dotson Ice Shelf. Residual tide and IBE signals contribute 22 m a^{-1} error to the across-track component of our stacked velocity solution. With the inclusion of other error terms, the total error in our map of velocity magnitude is at most 31 m a^{-1}. The technique of stacking is particularly well suited to areas where the accuracy of tide and atmospheric-pressure models is uncertain, such as remote regions of Antarctica where in situ validatory records are scarce. Even in regions where model accuracy is high, stacking will complement the removal of modelled tidal and IBE signals by further reducing residual signals, along with unwanted atmospheric, topographic and baseline effects. In the coming years, the launch of several satellite missions with short revisit times offers the prospect of regular sequences of SAR acquisitions. This study demonstrates that applying a stacking-based approach to these data can further improve estimates of ice-shelf flow.

8. ACKNOWLEDGEMENTS

This work was funded by the UK Natural Environment Research Council's National Centre for Earth Observation, through a Centre for Polar Observation and Modelling PhD studentship. We acknowledge the US National Snow and Ice Data Center (http://nsidc.org/) for providing the ICESat data, the British Atmospheric Data Centre for supplying the ECMWF data and the ESA VECTRA programme for

providing the raw SAR data. We thank Adrian Luckman and an anonymous reviewer for providing thoughtful reviews which helped to substantially improve the manuscript.

REFERENCES

Bamber JL and Bindschadler RA (1997) An improved elevation dataset for climate and ice-sheet modelling: validation with satellite imagery. *Ann. Glaciol.*, **25**, 439–444

Bamber J and Gomez-Dans JL (2005) The accuracy of digital elevation models of the Antarctic continent. *Earth Planet. Sci. Lett.*, **237**(3–4), 516–523

Bechor NBD and Zebker HA (2006) Measuring two-dimensional movements using a single InSAR pair. *Geophys. Res. Lett.*, **33**(16), L16311 (doi: 10.1029/2006GL026883)

Biggs J, Wright T, Lu Z and Parsons B (2007) Multi-interferogram method for measuring interseismic deformation: Denali Fault, Alaska. *Geophys. J. Int.*, **170**(3), 1165–1179 (doi: 10.1111/j.1365-246X.2007.03415.x)

Brenner AC and 10 others (2003) Derivation of range and range distributions from laser pulse waveform analysis for surface elevations, roughness, slope and vegetation heights. *Algorithm Theoretical Basis Document, Version 4.1*. NASA Goddard Space Flight Center, Greenbelt, MD (http://www.csr.utexas.edu/glas/pdf/Atbd_20031224.pdf)

De Angelis H and Skvarca P (2003) Glacier surge after ice shelf collapse. *Science*, **299**(5612), 1560–1562

Derauw D (1999) DInSAR and coherence tracking applied to glaciology: the example of Shirase Glacier. In Saway-Lacoste H ed. *Second International Workshop on SAR Interferometry 'FRINGE '99'. Advancing ERS SAR interferometry from applications towards operations, 10–12 November 1999, Liège, Belgium*. European Space Agency, Noordwijk (ESA SP-478)

Egbert GD, Bennett AF and Foreman MGG (1994) TOPEX/POSEIDON tides estimated using a global inverse model. *J. Geophys. Res.*, **99**(C12), 24 821–24 852

Emardson TR, Simons M and Webb FH (2003) Neutral atmospheric delay in interferometric synthetic aperture radar applications: statistical description and mitigation. *J. Geophys. Res.*, **108**(B5), 2231 (doi: 10.1029/2002JB001781)

Goldstein RM, Engelhardt H, Kamb B and Frolich RM (1993) Satellite radar interferometry for monitoring ice sheet motion: application to an Antarctic ice stream. *Science*, **262**(5139), 1525–1530

Gourmelen N and Amelung F (2005) Postseismic mantle relaxation in the Central Nevada seismic belt. *Science*, **310**(5753), 1473–1476 (doi: 10.1126/science.1119798)

Gourmelen N, Kim SW, Shepherd A, Park JW, Sundal AV and Björnsson H (2011) Ice velocity determined using conventional and multiple-aperture InSAR. *Earth Planet. Sci. Lett.*, **307**(1–2), 156–160

Gray AL, Mattar KE and Sofko G (2000) Influence of ionospheric electron density fluctuations on satellite radar interferometry. *Geophys. Res. Lett.*, **27**(10), 1451–1454

Haran T, Bohlander J, Scambos T, Painter T and Fahnestock M (2006) *MODIS mosaic of Antarctica (MOA) image map*. National Snow and Ice Data Center, Boulder, CO. Digital media: http://nsidc.org/data/nsidc-0280.html

Hartl P, Thiel KH, Wu X, Doake CSM and Sievers J (1994) Application of SAR interferometry with ERS-1 in the Antarctic. *Earth Obs. Q.*, **43**, 1–4

Jacobs SS, Hellmer HH and Jenkins A (1996) Antarctic ice sheet melting in the southeast Pacific. *Geophys. Res. Lett.*, **23**(9), 957–960

Jenkins A and 6 others (2010) Observations beneath Pine Island Glacier in West Antarctica and implications for its retreat. *Nature Geosci.*, **3**(7), 468–472

Joughin I and Padman L (2003) Melting and freezing beneath Filchner–Ronne Ice Shelf, Antarctica. *Geophys. Res. Lett.*, **30**(9), 1477–1480

Joughin IR, Winebrenner DP and Fahnestock MA (1995) Observations of ice-sheet motion in Greenland using satellite radar interferometry. *Geophys. Res. Lett.*, **22**(5), 571–574

Joughin I, Kwok R and Fahnestock M (1996) Estimation of ice-sheet motion using satellite radar interferometry: method and error analysis with application to Humboldt Glacier, Greenland. *J. Glaciol.*, **42**(142), 564–575

Joughin I, Rignot E, Rosanova CE, Lucchitta BK and Bohlander J (2003) Timing of recent accelerations of Pine Island Glacier, Antarctica. *Geophys. Res. Lett.*, **30**(13), 1706 (doi: 10.1029/2003GL017609)

Jung H-S, Won J-S and Kim S-W (2009) An improvement of the performance of multiple-aperture SAR interferometry (MAI). *IEEE Trans. Geosci. Remote Sens.*, **47**(8), 2859–2869

King MA and Padman L (2005) Accuracy assessment of ocean tide models around Antarctica. *Geophys. Res. Lett.*, **32**(23), L15601 (doi: 10.1029/2005GL023901)

King MA and 6 others (2011) Ocean tides in the Weddell Sea: new observations on the Filchner–Ronne and Larsen C ice shelves and model validation. *J. Geophys. Res.*, **116**(C6), C06006 (doi: 10.1029/2011JC006949)

Kwok R and Fahnestock MA (1996) Ice sheet motion and topography from radar interferometry. *IEEE Trans. Geosci. Remote Sens.*, **34**(1), 189–200

Lang O, Rabus BT and Dech SW (2004) Velocity map of the Thwaites Glacier catchment, West Antarctica. *J. Glaciol.*, **50**(168), 46–56

Lyard F, Lefevre F, Letellier T and Francis O (2006) Modelling the global ocean tides: modern insights from FES2004. *Ocean Dyn.*, **56**(5–6), 394–415

McMillan M, Shepherd A, Vaughan DG, Laxon S and McAdoo D (2009) Amundsen Sea bathymetry: the benefits of using gravity data for bathymetric prediction. *IEEE Trans. Geosci. Remote Sens.*, **47**(12), 4223–4228

McMillan M, Shepherd A, Nienow P and Leeson A (2011) Tide model accuracy in the Amundsen Sea, Antarctica, from radar interferometry observations of ice shelf motion. *J. Geophys. Res.*, **116**(C11), C11008 (doi: 10.1029/2011JC007294)

Nitsche FO, Jacobs SS, Larter RD and Gohl K (2007) Bathymetry of the Amundsen Sea continental shelf: implications for geology, oceanography, and glaciology. *Geochem. Geophys. Geosyst.*, **8**(Q10), Q10009 (doi: 10.1029/2007GC001694)

Padman L, Fricker HA, Coleman R, Howard S and Erofeeva L (2002) A new tide model for the Antarctic ice shelves and seas. *Ann. Glaciol.*, **34**, 247–254

Padman L, King M, Goring D, Corr H and Coleman R (2003) Ice-shelf elevation changes due to atmospheric pressure variations. *J. Glaciol.*, **49**(167), 521–526

Padman L, Erofeeva SY and Fricker HA (2008) Improving Antarctic tide models by assimilation of ICESat laser altimetry over ice shelves. *Geophys. Res. Lett.*, **35**(22), L22504 (doi: 10.1029/2008GL035592)

Pattyn F and Derauw D (2002) Ice-dynamic conditions of Shirase Glacier, Antarctica, inferred from ERS SAR interferometry. *J. Glaciol.*, **48**(163), 559–565

Payne AJ, Vieli A, Shepherd A, Wingham DJ and Rignot E (2004) Recent dramatic thinning of largest West Antarctic ice stream triggered by oceans. *Geophys. Res. Lett.*, **31**(23), L23401 (doi: 10.1029/2004GL021284)

Payne AJ, Holland PR, Shepherd AP, Rutt IC, Jenkins A and Joughin I (2007) Numerical modeling of ocean–ice interactions under Pine Island Bay's ice shelf. *J. Geophys. Res.*, **112**(C10), C10019 (doi: 10.1029/2006JC003733)

Pritchard HD, Arthern RJ, Vaughan DG and Edwards LA (2009) Extensive dynamic thinning on the margins of the Greenland and Antarctic ice sheets. *Nature*, **461**(7266), 971–975

Rignot E (1996) Tidal motion, ice velocity and melt rate of Petermann Gletscher, Greenland, measured from radar interferometry. *J. Glaciol.*, **42**(142), 476–485

Rignot EJ (1998) Fast recession of a West Antarctic glacier. *Science*, **281**(5376), 549–551

Rignot E (2002) Ice-shelf changes in Pine Island Bay, Antarctica, 1947–2000. *J. Glaciol.*, **48**(161), 247–256

Rignot E (2008) Changes in West Antarctic ice stream dynamics observed with ALOS PALSAR data. *Geophys. Res. Lett.*, **35**(12), L12505 (doi: 10.1029/2008GL033365)

Rignot E and Jacobs SS (2002) Rapid bottom melting widespread near Antarctic ice sheet grounding lines. *Science*, **296**(5575), 2020–2023

Rignot E and MacAyeal DR (1998) Ice-shelf dynamics near the front of the Filchner–Ronne Ice Shelf, Antarctica, revealed by SAR interferometry. *J. Glaciol.*, **44**(147), 405–418

Rignot E, Padman L, MacAyeal DR and Schmeltz M (2000) Observation of ocean tides below the Filchner and Ronne Ice Shelves, Antarctica, using synthetic aperture radar interferometry: comparison with tide model predictions. *J. Geophys. Res.*, **105**(C8), 19 615–19 630

Rignot E, Casassa G, Gogineni P, Krabill W, Rivera A and Thomas R (2004) Accelerated ice discharge from the Antarctic Peninsula following the collapse of Larsen B ice shelf. *Geophys. Res. Lett.*, **31**(18), L18401 (doi: 10.1029/2004GL020697)

Rignot E and 9 others (2005) Recent ice loss from the Fleming and other glaciers, Wordie Bay, West Antarctic Peninsula. *Geophys. Res. Lett.*, **32**(7), L07502 (doi: 10.1029/2004GL021947)

Rignot E and 6 others (2008) Recent Antarctic ice mass loss from radar interferometry and regional climate modelling. *Nature Geosci.*, **1**(2), 106–110

Rodriguez E and Martin JM (1992) Theory and design of interferometric synthetic aperture radars. *IEE Proc. F*, **139**(2), 147–159

Rott H, Rack W, Skvarca P and De Angelis H (2002) Northern Larsen Ice Shelf, Antarctica: further retreat after collapse. *Ann. Glaciol.*, **34**, 277–282

Sandwell DT and Price EJ (1998) Phase gradient approach to stacking interferograms. *J. Geophys. Res.*, **103**(B12), 30 183–30 204

Sandwell DT and Sichoix L (2000) Topographic phase recovery from stacked ERS interferometry and a low-resolution digital elevation model. *J. Geophys. Res.*, **105**(B12), 28 211–28 222

Scambos TA, Bohlander JA, Shuman CA and Skvarca P (2004) Glacier acceleration and thinning after ice shelf collapse in the Larsen B embayment, Antarctica. *Geophys. Res. Lett.*, **31**(18), L18402 (doi: 10.1029/2004GL020670)

Shepherd A and Peacock NR (2003) Ice shelf tidal motion derived from ERS altimetry. *J. Geophys. Res.*, **108**(C6), 3198 (doi: 10.1029/2001JC001152)

Shepherd A and Wingham D (2007) Recent sea-level contributions of the Antarctic and Greenland ice sheets. *Science*, **315**(5818), 1529–1532

Shepherd A, Wingham D and Mansley JA (2002) Inland thinning of the Amundsen Sea sector, West Antarctica. *Geophys. Res. Lett.*, **29**(10), 1364 (doi: 10.1029/2001GL014183)

Shepherd A, Wingham D and Rignot E (2004) Warm ocean is eroding West Antarctic Ice Sheet. *Geophys. Res. Lett.*, **31**(23), L23404 (doi: 10.1029/2004GL021106)

Strozzi T, Luckman A, Murray T, Wegmuller U and Werner CL (2002) Glacier motion estimation using satellite-radar offset-tracking procedures. *IEEE Trans. Geosci. Remote Sens.*, **40**(11), 2834–2391

Thoma M, Jenkins A, Holland D and Jacobs S (2008) Modelling Circumpolar Deep Water Intrusions on the Amundsen Sea continental shelf, Antarctica. *Geophys. Res. Lett.*, **35**(18), L18602 (doi: 10.1029/2008GL034939)

Uppala SM and 45 others (2005) The ERA-40 re-analysis. *Q. J. R. Meteorol. Soc.*, **131**(612), 2961–3012

Vaughan DG and Doake CSM (1996) Recent atmospheric warming and retreat of ice shelves on the Antarctic Peninsula. *Nature*, **379**(6563), 328–331

Vieli A, Payne AJ, Du Z and Shepherd A (2006) Numerical modelling and data assimilation of the Larsen B ice shelf, Antarctic Peninsula. *Philos. Trans. R. Soc. London, Ser. A*, **364**(1844), 1815–1839

Vieli A, Payne AJ, Shepherd A and Du Z (2007) Causes of pre-collapse changes of the Larsen B ice shelf: numerical modelling and assimilation of satellite observations. *Earth Planet. Sci. Lett.*, **259**(3–4), 297–306

Werner LC, Wegmüller U, Strozzi T and Wiesmann A (2001) Gamma SAR and interferometric processing software. In *Proceedings of ERS-ENVISAT Symposium, 16–20 October 2000, Gothenburg, Sweden*. European Space Agency, Noordwijk, 16–20 (ESA SP-461)

Wingham DJ, Wallis DW and Shepherd A (2009) Spatial and temporal evolution of Pine Island Glacier thinning, 1995–2006. *Geophys. Res. Lett.*, **36**(17), L17501 (doi: 10.1029/2009GL039126)

Wright T, Parsons B and Fielding E (2001) Measurement of interseismic strain accumulation across the North Anatolian Fault by satellite radar interferometry. *Geophys. Res. Lett.*, **28**(10), 2117–2120

Zebker HA, Rosen PA and Hensley S (1997) Atmospheric effects in interferometric synthetic aperture radar surface deformation and topographic maps. *J. Geophys. Res.*, **102**(B4), 7547–7563

Zwally HJ and 15 others (2002) ICESat's laser measurements of polar ice, atmosphere, ocean and land. *J. Geodyn.*, **34**(3–4), 405–445

MS received 21 April 2011 and accepted in revised form 17 November 2011